A Fully Transparent and Flexible Ultraviolet–Visible Photodetector Based on Controlled Electrospun ZnO-CdO Heterojunction Nanofiber Arrays

*Zhi Zheng, Lin Gan, Huiqiao Li, Ying Ma, Yoshio Bando, Dmitri Golberg, and Tianyou Zhai**

It is essential for novel photodetectors to show good photoresponses, high stability, and have facile fabrication methods. Herein, an optimized electrospinning method to fabricate a photodetector based on nanowire arrays that has a wide spectral response range is demonstrated. Arrays of ZnO-CdO hybrid nanowires are carefully fabricated fusing ZnO and CdO portions into the same nanowires and subsequently assembling those nanowires into a regular structure. Compared to pure ZnO or CdO nanowire arrays, the hybrid arrays show comparable photocurrent/dark current ratios and response speeds, but they possess a much wider spectral response range from ultraviolet to visible light. The optoelectronic and electronic properties of the ZnO-CdO hybrid nanowire arrays are systematically explored. Based on this, a transparent and flexible photodetector made of ZnO-CdO hybrid nanowire arrays is fabricated. It shows a high transparency of around 95% in the spectral range of 400–800 nm and maintains its properties even after 200 bending cycles. Importantly, the developed, simple method can be directly applied to many types of substrates and a transfer of the nanowires becomes unnecessary, which guarantees a high quality of the devices.

1. Introduction

Low-dimensional materials, because of their high surface area to volume ratios, wide range of spectral responses, plentiful categories, etc.[1–5] have wide applications in optoelectronics, including imaging, night-time surveillance, environmental monitoring, target identification and defense sensing. Generally, such materials have a high selectivity for a specific wavelength according to their bandgaps. For example, $In_2Ge_2O_7$ (4.4 eV) and Ga_2O_3 (4.9 eV) nanowires showed a good performance for detection in the deep ultraviolet;[6] ZnO (3.4 eV), SnO_2 (3.6 eV), In_2O_3 (3.6 eV), and Nb_2O_5 (3.4 eV) nanowires are sensitive to ultraviolet light[7–11] CdS (2.4 eV), ZnTe (2.4 eV), and In_2S_3 (2.0 eV) nanowires work well in the visible spectral range and InAs (0.35 eV) and Cd_3P_2 (0.65 eV) nanowires play a vital roles in near-infrared light detection.[12–16] Interestingly, these days, photodetectors with a broad spectral response have started to attract more and more attention because as such a "multicolor" response can be realized in a single photodetector.[17,18] Currently, there are two ways to achieve such a response: one is to form an alloy, for instance $(Al, In)_xGa_{(1-x)}N$, which has a tunable response range from the near-ultraviolet to near-infrared light;[19,20] another is to form hybrid structures, such as CdSe/ZnTe core–shell structures,[21] ZnS/ZnO biaxial structures[22] or quantum dots/organic mixtures,[23–25] which combine the spectral response range of their constituting components. However, the low stability or complex fabrication requirements prevent the wide spread of such "multicolor" materials. According to the "6S" criteria for evaluating photodetectors, that is, high spectral selectivity, high signal-to-noise ratio, high sensitivity, high stability, high speed, and simplicity for fabrication, the realization of a highly stable, simply processed photodetector is still an issue to be considered.[26]

Electrospinning is a cheap and facile method to fabricate various nanofibers on a large scale. This has been widely utilized for supercapacitors, lithium-ion batteries, photocatalysis, etc.[27,28] Specifically, the target material is mixed with a polymer first to form a uniform solution, and then the solution is expelled out of the vessel by an ejector jet pump. At the same time, a high voltage is applied between the outlet of the vessel and the collecting substrate, which endows the exposed solution with a charge and provides a strong field to transform the solution into thin nanofibers of tens to hundreds of nanometers in diameter. Finally, all the nanofibers are collected on the substrate. It is worth mentioning that the product is generally composed of a huge number of random nanofibers. In contrast, uniform nanofiber arrays can be achieved by putting separated electrodes on the substrate during the electrospinning

Z. Zheng, Dr. L. Gan, Dr. H. Q. Li, Prof. Y. Ma, Prof. T. Y. Zhai
State Key Laboratory of Material Processing and Die & Mould Technology
School of Materials Science and Engineering
Huazhong University of Science and Technology (HUST)
Wuhan 430074, P. R. China
E-mail: zhaity@hust.edu.cn
Prof. Y. Bando, Prof. D. Golberg
International Center for Materials Nanoarchitectonics (MANA)
National Institute for Materials Science (NIMS)
Namiki 1-1, Tsukuba, Ibaraki 305-0044, Japan

DOI: 10.1002/adfm.201502499

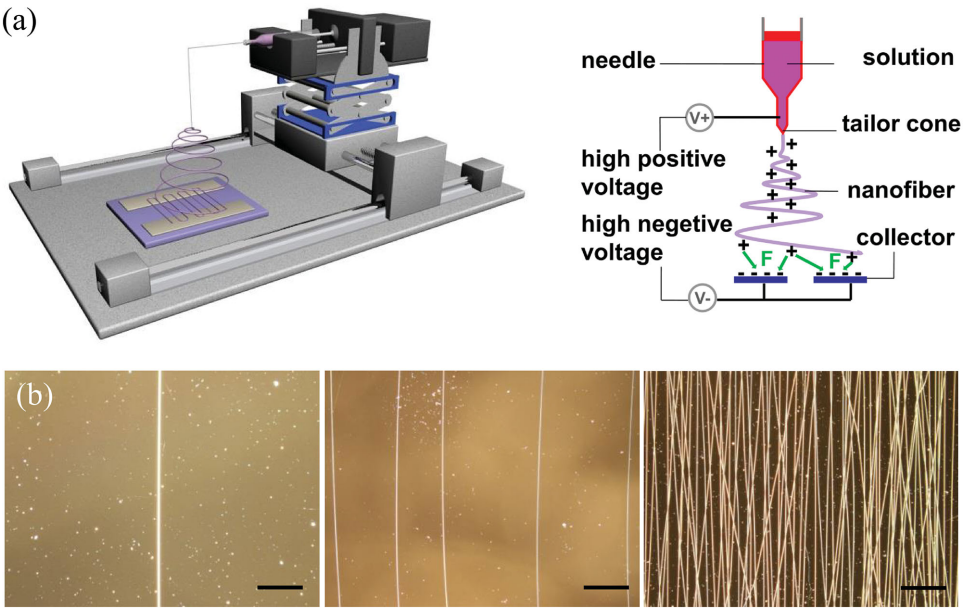

Figure 1. Fabrication of nanofibers via an optimized electrospinning method. a) Setup of the electrospinning machine. Two separated electrodes instead of a common insulator are used as the collectors, which forces the nanofibers to become straight after the process. b) Optical images of well-aligned nanofibers with different densities on the substrate. Scale bar: 100 μm.

process.[29–32] The mechanism of nanofibers that are assembled by using separated electrodes is shown in **Figure 1**a, in which two electrodes give the nanofibers a pulling force to keep them straight; and the charge on the nanofibers separates them from each other because of electric repulsion. As a result, tunable nanofiber arrays can be realized using a setup shown in Figure 1b. Moreover, more complex array configurations may be prepared by rotating the electrodes. This technique is transfer-free, which is another major advantage of electrospinning, that is, the sample is directly deposited on the target substrate (any type of insulator, such as mica, quartz, etc.) without the need for further wire-transfer operations, which simplifies the fabrication process and ensures a high quality of the final product.

Metal oxides are common minerals on Earth, they show an excellent stability in air at ambient conditions and even under a relatively high temperature.[33] They are easily processable via simple sintering and can be shaped as nanofibers after electrospinning in air. In this work, we investigated the optoelectronic and electronic properties of ZnO and CdO hybrid nanofiber array (NFA) structures fabricated by electrospinning. Two types of metal oxides were fused (sintering under 500 °C) into individual nanofibers and were assembled into arrays under an electric field, then the array performance was explored in a flexible and transparent photodetector configuration. ZnO and CdO have complementary bandgaps corresponding to the ultraviolet and visible light ranges, respectively, ensuring that the hybrid structure has a wide response range, from the visible to the ultraviolet. Temperature-dependent analysis revealed that this hybrid NFA was a typical semiconductor with plenty of oxygen vacancies. Its electronic characteristics could be well described by a thermal activation model. Moreover, taking advantage of the transfer-free technology involved, a flexible and transparent hybrid-NFA-based photodetector was fabricated directly on a mica substrate (the relatively high sintering temperature requires substrates with a certain thermal resistance).[34–36] The final photodetector had a transparency of approximately 95% and maintained its optoelectronic properties even after 200 bending cycles.

2. Results and Discussion

2.1. The Morphology and Structure of the NFA

Three types of NFA were fabricated via an improved electrospinning method,[37] in which two separated electrodes on the collector force the orderly assembly of the nanofibers under a high voltage applied between the collector and the vessel outlet (Figure 1b). The direction of the arrays could be adjusted by rotation of the electrodes, therefore, different types of arrays could easily be fabricated (Figure S1, Supporting Information). The precursors were mixed with a solution of polyvinylpyrrolidone (PVP) dissolved in dimethyl formamide (DMF) before electrospinning and after NFA forming they were annealed in air to remove excess PVP. In **Figure 2**a–c the optical images of ZnO, CdO, and ZnO-CdO hybrid NFA are illustrated, respectively. All nanofibers were assembled side by side to form a uniform film. The density of the NFA was tunable by varying the electrospinning parameter, such as the rate of precursor feeding and the electrospinning time. The composition of the NFA was identified using X-ray diffraction (XRD), as demonstrated in Figure 2d. The XRD spectra of the samples in Figure 2a,b matched that of standard ZnO (JCPDS No. 36-1451) and CdO (JCPDS No. 05-0640), respectively, evidencing pure hexagonal ZnO and cubic CdO structures. For the hybrid sample in Figure 2c, which was made using two kinds of precursors, the XRD spectra showed a combination of the two types of metal

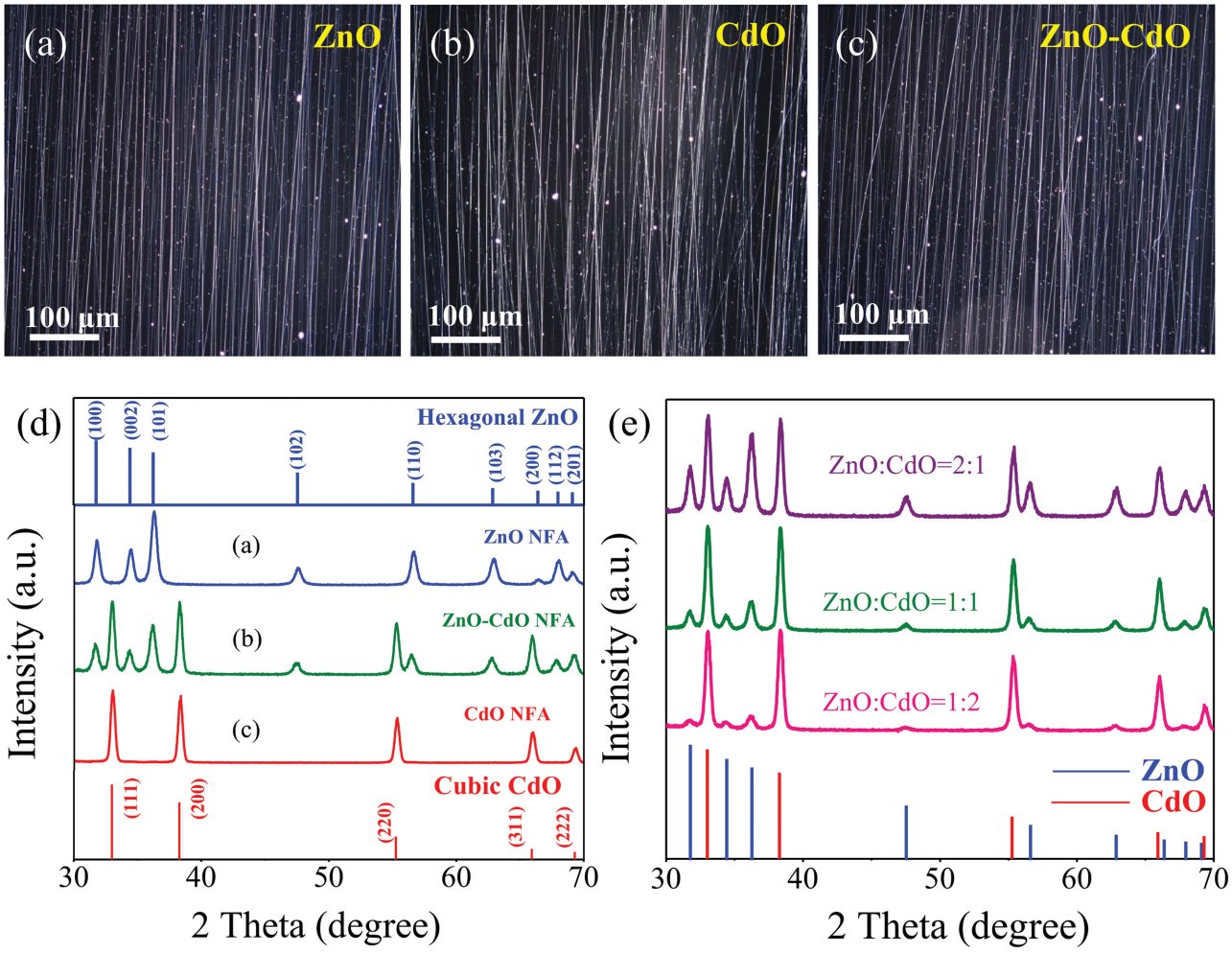

Figure 2. Three types of nanofiber arrays fabricated with optimized electrospinning. Optical images for a) ZnO, b) CdO, and c) ZnO-CdO hybrid nanofiber arrays. d) XRD spectra of the three types of nanofiber arrays. e) Comparison of XRD spectra for ZnO-CdO hybrid nanofiber arrays having various ratios of ZnO and CdO.

oxides, namely, ZnO and CdO. It is worth noting that the XRD of the hybrid structure did not show any extra peaks, except those of ZnO and CdO, suggesting that the hybrid structure contains only pure ZnO and CdO phases and no alloying had occurred. To test this point, various recipes of precursors were prepared and checked by XRD after sintering in air. As shown in Figure 2e, the three recipes only led to a difference in the intensity of the peaks, which can be attributed to the different quantities of precursors. However, for all three recipes, no new peaks were observed.

To further confirm the structure of NFA, a single nanofiber was investigated under transmission electron microscopy (TEM). As shown in **Figure 3**a, the ZnO nanofiber has a diameter of around 100 nm. It keeps its linear form after sintering, suggesting that high-temperature sintering has little influence on the fiber morphology. Figure 3b displays a well-resolved periodical lattice image with a 0.28 nm fringe separation, evidencing that the facet belongs to the (100) planes of hexagonal ZnO. The whole ZnO nanofiber was composed of a large number of small-sized ZnO nanocrystals, as revealed by selected-area electron diffraction (SAED) (Figure 3c). Different planes of the ZnO crystal in the nanofiber can be identified when looking at the diffraction rings, proving its polycrystalline structure. The same was found for the CdO nanofibers, where the fringe separation of 0.27 nm in the HRTEM image corresponded to the (111) planes of cubic CdO. The diffraction rings in the SAED pattern also evidenced that the whole nanofiber consisted of a large number of small-sized CdO nanocrystals. Moreover, based on both HRTEM images, no porous carbon coating was found on the nanofibers, suggesting that the PVP had been effectively removed under post-processing and the whole nanofiber consisted of pure metal oxides. For the hybrid sample (**Figure 4**a), the whole nanofiber was composed of CdO and ZnO nanocrystals mixture, which is supported by the HRTEM image in Figure 4b. The lattice-fringe separations of 0.24 nm and 0.27 nm were identified as the (101) planes of hexagonal ZnO and the (111) planes of cubic CdO, respectively. The mole ratio of Zn and Cd ions was around 1 (Figure 4c). The slight carbon signal might come from the supporting carbon film on the TEM grid and the tiny residue of amorphous carbon in the sintered nanofibers. The elemental distribution within the whole nanofiber was studied by energy dispersive X-ray

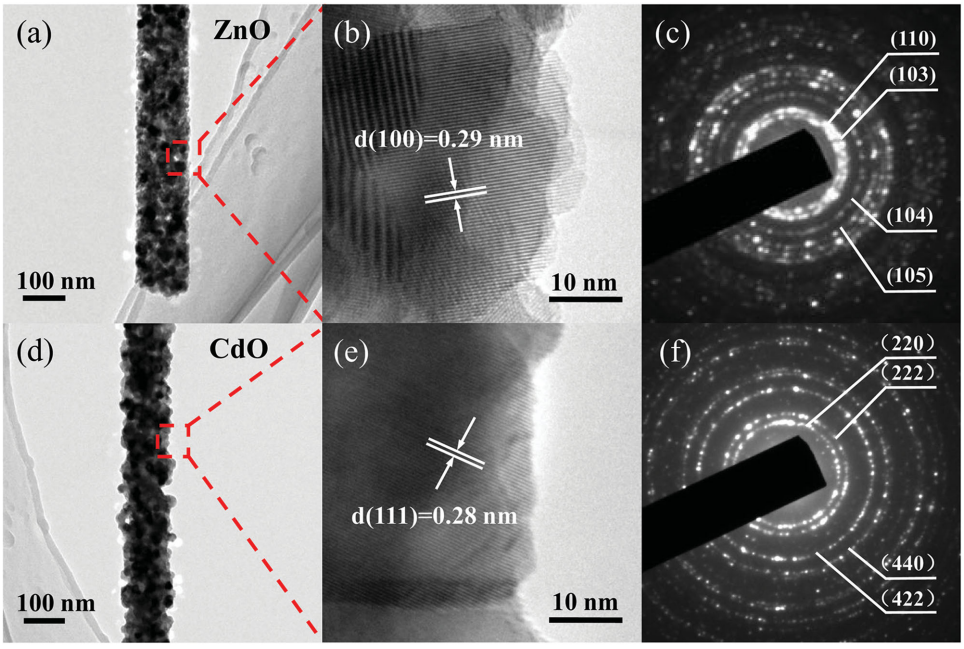

Figure 3. TEM images of bare nanofibers. a–c) TEM image, HRTEM image, and SAED pattern, respectively, for an individual ZnO nanofiber. d–f) TEM image, HRTEM image, and SAED pattern, respectively, of an individual CdO nanofiber.

spectroscopy (EDS) mapping, as shown in Figure 4d-f. It can be seen that all elements, namely Zn, Cd, and O are uniformly dispersed along the nanofiber, revealing that the ZnO and CdO nanoparticles have been evenly mixed rather than aggregated into isolated large-size homogeneous particles. The uniform dispersion of ZnO and CdO domains in the nanofiber ensures the reproducibility of the technique.

2.2. Optoelectronic Properties of NFA under a 325-nm Laser

To further explore the optoelectronic properties of the NFA, a simple two-electrode device configuration was adopted to make three types of NFA, based on ZnO, CdO, and ZnO-CdO NFA, respectively. The devices were fabricated on 500-nm SiO_2/Si and Ti/Au contacts were deposited to serve as the two

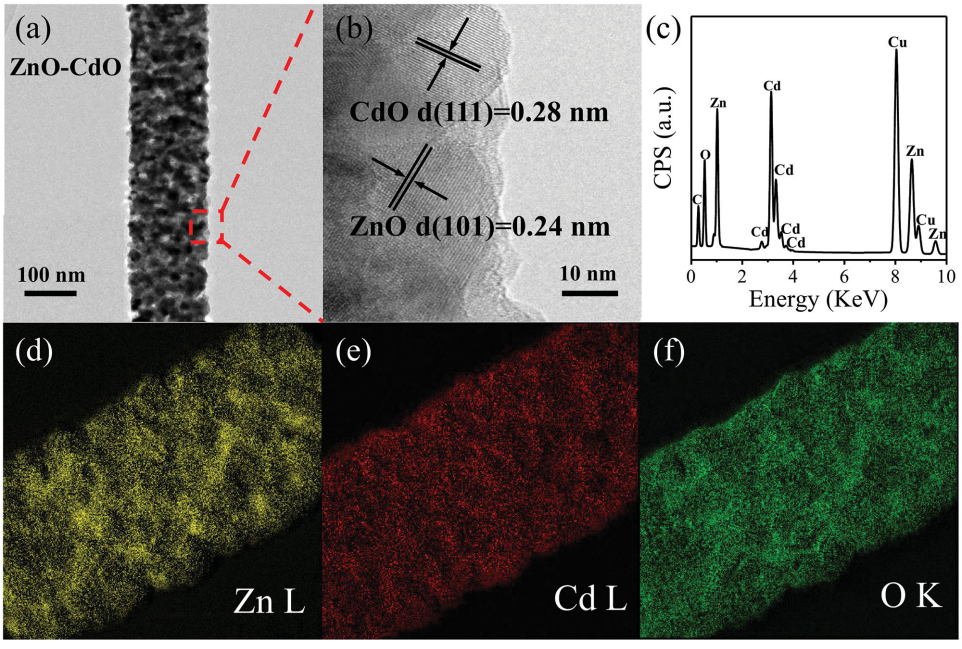

Figure 4. a,b) TEM and HRTEM images of a hybrid ZnO-CdO nanofiber. c) EDS spectrum of the hybrid nanofiber; d–f) Spatially-resolved EDS elemental maps of the Zn, Cd, and O species, respectively, in the hybrid nanofiber.

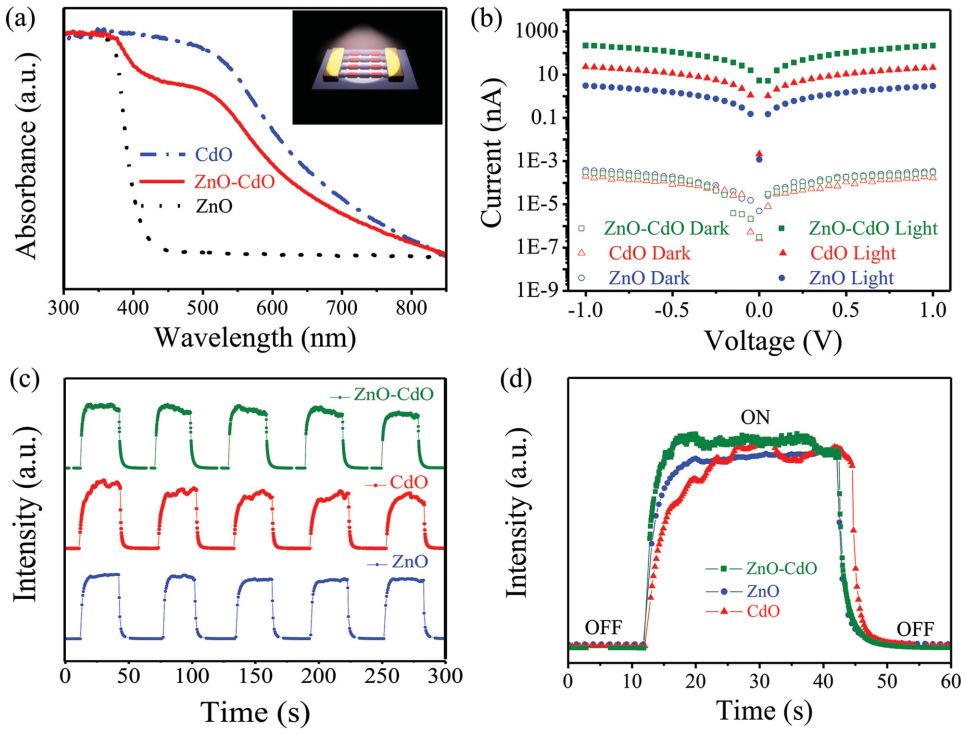

Figure 5. Optoelectronic properties of nanofiber arrays. a) UV–vis diffuse reflectance curves of three types of nanofiber arrays, the inset is the experimental setup showing the device configuration. b) Current–voltage (*I–V*) curves of the three types of devices under 325-nm laser illumination and in the dark. c) Current–time (*I–t*) curves of the three types of devices during on-off switching tests under 325-nm laser illumination. d) Comparison of the response time of the three types of devices.

electrodes covering both ends of the NFA, the device configuration is shown in the inset of **Figure 5**a. The UV–vis diffuse reflectance curves of the three types of NFA are demonstrated in Figure 5a. As can be seen, the ZnO shows a stable horizontal line from 850 nm to 450 nm, and then a sharp peak arises where the wavelength of the incident light becomes shorter than 450 nm, which coincides with the bandgap of ZnO (3.4 eV).[38] The case of CdO is similar to that of ZnO, the only difference is that the threshold wavelength for CdO is 550 nm, meaning that light with a wavelength shorter than 550 nm would be extensively absorbed by the CdO nanofiber. For the hybrid nanofiber consisting of ZnO-CdO, the curve seems to reflect the combination of those of ZnO and CdO, it has two absorbance bands located at around 350 nm and 550 nm, corresponding to the bandgaps of ZnO and CdO, respectively. Therefore, we can conclude that the hybrid nanofiber combines the spectral response of its components.[39] In accordance with these UV–vis diffuse reflectance curves, a 325-nm laser was chosen to excite the three NFA samples and their photocurrent curves are depicted in Figure 5b. The highly symmetrical shape of the current curves evidences a good Ohmic contact between NFA and the electrodes (Figure S2, Supporting Information). The difference between the photocurrent under 325-nm light and that in the dark of the three NFA samples can be as high as 10^4–10^5 times, suggesting the high quality of the NFAs. These data are also summarized in Table S1 in the Supporting Information. Generally, comparable high photocurrent/dark-current ratios result from a low dark current.[40] In a ZnO-CdO NFA the whole hybrid nanofiber is composed of a large number of ZnO and CdO nanoparticles (see Figure 4b), suggesting a huge number of interfaces in the hybrid nanofiber; this would suppress the dark current effectively. In the meantime, the small-nanoparticles structure enhances the absorption of the incident light, therefore, the photocurrent could be improved as well. Although the hybrid sample showed the largest photocurrent of the three devices, this does not necessarily mean that the hybrid nanofiber has a better conductivity because the photocurrent is strongly dependent on the amount of nanofibers in the device. Figure 5c demonstrates the stability of the photoresponse in the three NFAs. Therefore, we subjected all three samples to ON/OFF switching with 325-nm laser illumination. During the 5 cycles of the switching test, which lasted over 300 s, the photoresponse in the three NFA samples showed a good stability, confirming the robustness of the metal oxide nanofibers. The response speed during ON/OFF tests is illustrated in Figure 5c. As shown in Figure 5d, in which a single ON/OFF process for each device is shown, the rise and decay curves in the three samples are comparable. Interestingly, the response speed of the ZnO-CdO hybrid NFA, was about 3 s and it did not show any degradation compared to those of the ZnO and CdO NFAs, suggesting that the heterogeneous interfaces between the ZnO and CdO nanoparticles in the hybrid nanofiber had no detrimental effect on the carrier transport compared to the homogeneous interfaces in the ZnO and CdO nanoparticles. In short, the ZnO-CdO hybrid NFA has a comparable response speed to that of ZnO or CdO NFAs but possesses a wider spectral response range than its single components.

To explore the reason behind this good performance of the ZnO-CdO hybrid NFA, a disordered ZnO-CdO nanofibers

(DNF) film was prepared via conventional electrospinning, in other words, without the separate electrodes on the collector. The stability of the photoresponse for the DNF and NFA is demonstrated in Figure S3a (Supporting Information). The two types of film showed a good stability during the 300-s ON/OFF switching tests under 325-nm laser illumination. However, the response speed was obviously different. For the DNF, the rise of the photocurrent was relatively slow, it took around 30 s to reach a stable current, in contrast, only about 3 s were required for the NFA to reach a stable current. A similar situation was apparent for the decay curves, suggesting that the carrier transport is different in the two types of films. More accurate photocurrent rise and decay times were acquired by fitting of the photoresponse curves, the detailed information for this can be found in Figure S4 (Supporting Information). We could thus attribute the fast response speed of NFA to its ordered arrangement in which almost all nanofibers were straight and assembled in a side-by-side fashion, which ensured that the carriers could travel through the shortest channels (Figure S3d,f in the Supporting Information).[41] However, for the DNF film, all nanofibers were coiled after electrospinning and stacked into a film in a random way, thereby creating a complex crossed network (Figure S3c,e in the Supporting Information). Therefore, the carriers in DNF have to travel over much longer channels. In addition, a huge number of cross junctions in the nanofiber network can scatter the carriers and further increase the transport time between two electrodes. As a result, compared to the ZnO-CdO DNF, ZnO-CdO NFA has the same merit of high stability but also had an obvious advantage with respect to the response speed.

2.3. Optoelectronic Properties of ZnO-CdO NFA

To systematically explore the optoelectronic properties of the ZnO-CdO NFA, we further studied its photoresponse with incident light of various wavelengths, various intensities, and at various pressures. In **Figure 6**a the photocurrent curves under dark conditions, 250-nm, 300-nm, 350-nm, 450-nm, and 550-nm light are depicted. All plots exhibited straight lines, suggesting a good Ohmic contact between the NFA and the electrodes. The dark current was maintained at a low level and the photocurrent under 550-nm irradiation was close to that under dark conditions. However, for the rest of the photocurrent curves, a larger photocurrent can clearly be observed. The largest photocurrent was recorded under 300-nm illumination. This result is consistent with the spectral response curves shown in Figure 5a in which the ZnO-CdO NFA has a response to incident light with a wavelength shorter than 550 nm, corresponding to the bandgap of CdO in the hybrid nanofiber. The logarithmic plot corresponding to Figure 6a is presented in Figure 6b, from which it can be seen that the hybrid nanofiber has the best response under 300-nm irradiation. Therefore, the following tests were based on a 2-mm diameter, 300-nm incident light with an intensity of 6.54 mW cm^{-2}. Considering the small NFA area (see caption of Figure 6), a responsivity of around 1 A W^{-1} could be calculated. Moreover, the photoresponse of hybrid NFA under 300-nm light at various intensities was measured and is illustrated in Figure 6c. As expected, higher light intensities induced higher photocurrents. The relation between the photocurrent and the light intensity (Figure 6d) could be fitted with a power law, $I_p \sim P^{\theta}$, in which I_p stands for a non-unity exponent relation with the incident light intensity, P. The non-unity exponent, θ, could be retrieved from the fitting to be 0.73, corresponding to the complex processes in a semiconductor, including electron–hole generation, separation, trapping, recombination, etc.[42] Furthermore, the photoresponse of hybrid NFA was additionally studied at various pressures, that is, under ambient atmosphere and in vacuum. The photocurrent responses in darkness and under 300-nm light were evaluated for both cases and it was seen that the hybrid NFA revealed a much larger current in vacuum than in air, suggesting that oxygen plays an important role in the carrier transport. Generally, oxygen from the air is adsorbed on the NFA surface, further acting as a trapping center for holes. As a result, the carrier concentration is lowered, leading to a lower current compared to that in vacuum. The obvious photoresponse difference between ambient atmosphere and vacuum strongly supports the above-mentioned oxygen-assisted photoresponse mechanism. Moreover, similar to oxygen, the humidity also plays an important role in the photoresponse process. A higher humidity was beneficial to the response rate but degraded the photocurrent, which is in accord with previously reported work.[43–45] The photoresponse data of the device under various humidities is demonstrated in Figure S5 (Supporting Information).

2.4. Electronic Transport Mechanism of ZnO-CdO NFA

The electronic properties of hybrid NFA were then investigated under various temperatures. As shown in **Figure 7**a, the current–voltage curves of the hybrid NFA were recorded between 60 K–430 K in vacuum; the optical image of the device is shown in the inset. It can be seen that the current increases with increasing temperature, demonstrating the typical behavior of a semiconductor. More information can be gained from the conductivity, σ, vs. the reciprocal temperature, $1000/T$, curve of the hybrid NFA, as presented in Figure 7b. The curve displays two distinct slopes for two temperature regimes, that is 430 K–220 K and 140 K–60 K, corresponding to a typical Arrhenius-type behavior and suggesting that the carrier transport is dictated by the thermal activation conduction processes.[46] All data can be well fitted (least-square fit) using the activation energy equation:[47]

$$\sigma = \sigma_1 \exp\left(-\frac{E_1}{k_B T}\right) + \sigma_2 \exp\left(-\frac{E_2}{k_B T}\right) \quad (1)$$

Where σ_1 and σ_2 are temperature-insensitive conductivity prefactors relevant to the activation energy during the thermal activation conduction processes, k_B is the Boltzmann constant, and T is the absolute temperature. Based on the fitting results, the σ_1, σ_2, E_1, and E_2 were calculated to be 53.9 fS, 0.341 fS, 116 meV, and 0.83 meV, respectively. Here the activation energy E_1 (116 meV) corresponds to a group of intermediately deep donors in the hybrid NFA and accordingly, E_2 (0.83 meV) represents a group of shallow donors in the hybrid NFA. Such low E_2 energy suggests that a large amount of oxygen vacancies exist in the hybrid NFA. This is reasonable given the polycrystalline

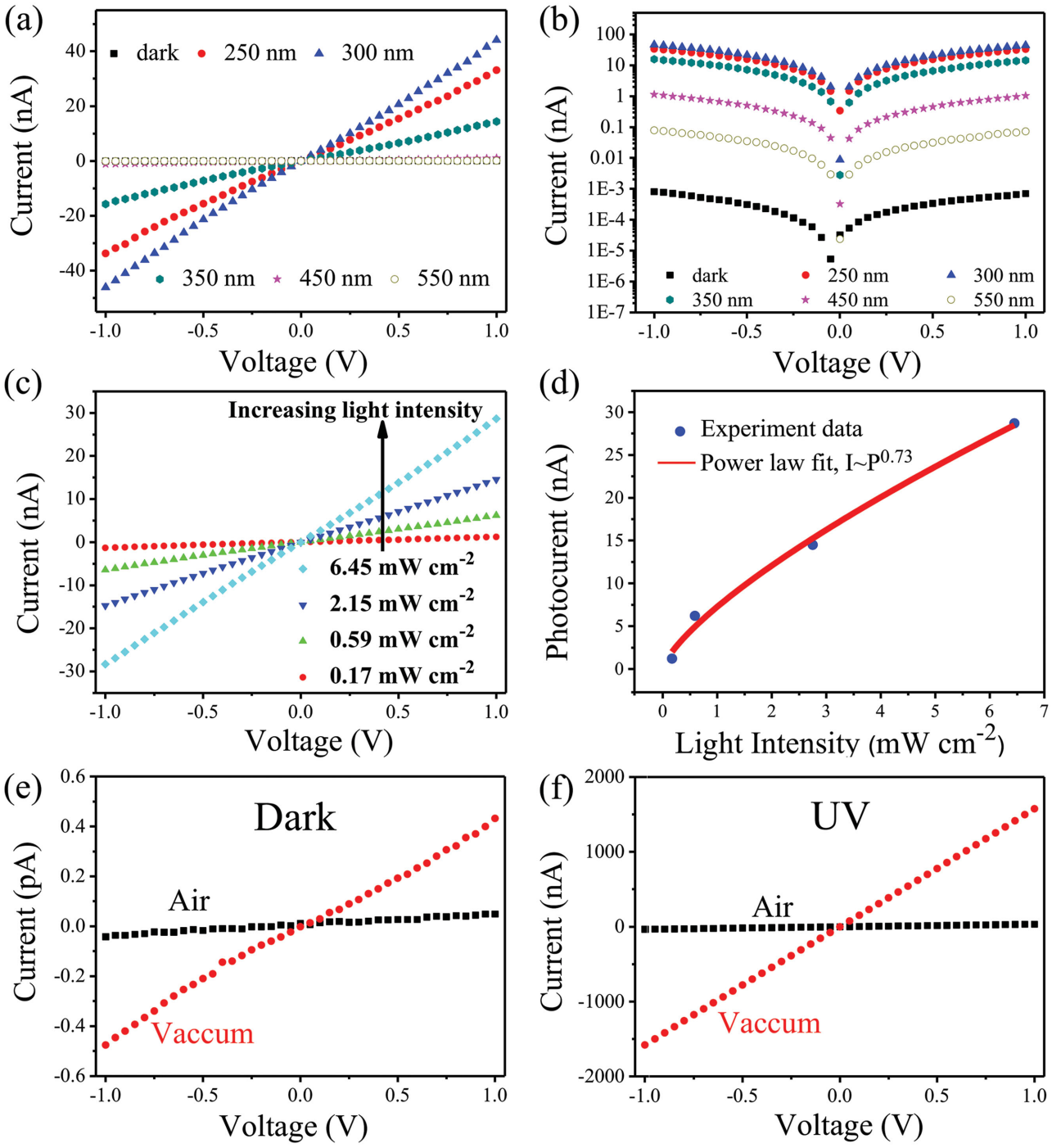

Figure 6. Optoelectronic properties of hybrid nanofiber arrays studied under light of various wavelengths. a) Current–voltage (*I–V*) curves of the device illuminated with light of various wavelengths and in the dark; b) Logarithmic plot of (a); c) Current–voltage (*I–V*) curves of the device illuminated under 300-nm light at various power intensities; d) Photocurrent as a function of light intensity and corresponding fitting curve using the power law under 300-nm light illumination. The power density of the incident light was 6.54 mW cm^2 and the light size was a round shape of 2 mm in diameter. The channel (30 μm in length and 500 μm in width) consisted of ca. 150 nanofibers with an average diameter of ca. 150 nm. e–f) Current–voltage (*I–V*) curves in the dark and under 300-nm light in air and vacuum.

nature of the hybrid NFA. In the higher temperature regime (430 K–220 K), the final conductivity reflects the combination of both the shallow and the intermediately deep donors contributions in which both types of donors exit to the conduction band with the aid of thermal energy.[48] However, the contribution of intermediately deep donors dominates the final conductivity. In contrast, in the lower temperature regime (140 K–60 K), the final conductivity is governed by the shallow donors. Therefore,

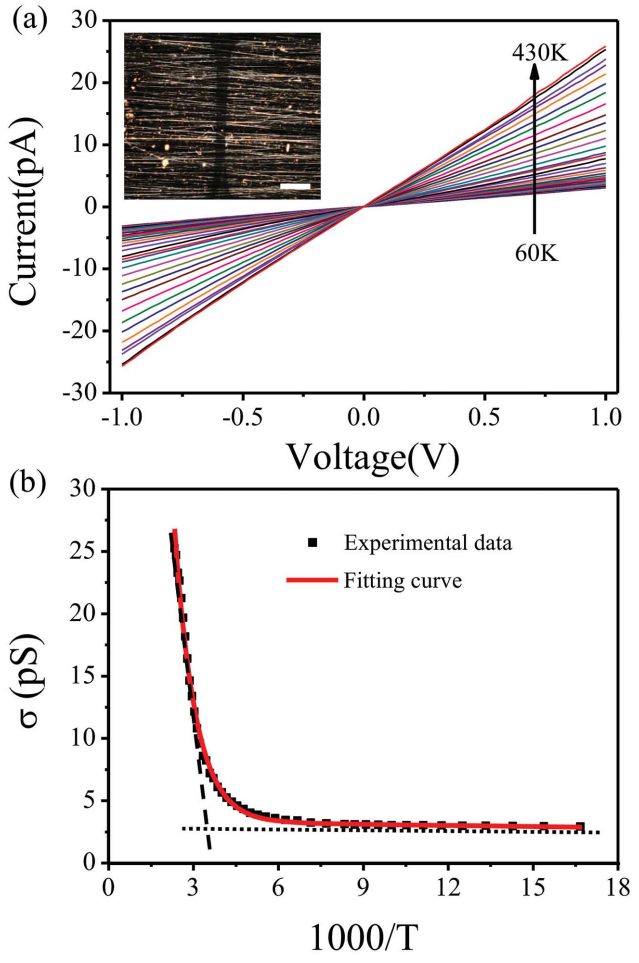

Figure 7. Electronic properties of hybrid nanofiber arrays. a) Current–voltage (*I–V*) curves of hybrid nanofiber arrays in the temperature range of 60–430 K, the scale bar is 50 μm. b) Dependence of conductivity, σ, on the reciprocal temperature, 1000/*T*.

the whole temperature dependence of the conductivity of the hybrid NFA can be well described using Equation (1), which corresponds to the "band conduction" processes.

3. Applications

Flexible devices based on this type of nanofibers have attracted wide interest globally.[49] Moreover, their transparency is another important parameter for various applications.[50] Based on the facile electrospinning technique and high performance of the ZnO-CdO NFAs, we fabricated a flexible, transparent photodetector on a mica substrate. As shown in **Figure 8**a, the logo of Huazhong University of Science and Technology (HUST) can be seen clearly beneath the transparent photodetector. The electrode arrays (50-nm ITO) and a thin layer of hybrid NFA (ca. 150 nm) were assembled on the mica substrate (ca. 40 μm). The photodetector had a high transparency, about 95%, over a wide wavelength range from 400 nm to 800 nm (Figure 8b). Considering the natural transparency of the mica substrate (ca. 95%), the light absorption of the hybrid NFA layer (ca. 150 nm) is negligible, indicating that the transparency of the photodetector is dictated by the mica substrate. The presence of the hybrid NFA has thus very little influence on the overall transparency. The hybrid NFA can be utilized effectively in this case, whereby the fiber arrays are mainly located at the predesigned sites. Moreover, as demonstrated in Figure 8c and 8d, the photodetector has an excellent flexibility. It can withstand a bending radius of 10 mm while maintaining its original properties. Durability tests indicated that the properties of this photodetector were well maintained even after 200 bending cycles.[51] It is worth mentioning that the transparency is strongly related to the substrate thickness and, thus, photodetectors of better transparency and flexibility can be realized by using thinner substrates. Considering the mechanism of the electrospinning process, the substrate or collector can also be replaced by different kinds of materials, which would further extend the applications of photodetectors.[52]

4. Conclusions

We have demonstrated a facile electrospinning method to fabricate a flexible, transparent photodetector with a wide spectral response range based on ZnO-CdO hybrid nanofiber arrays, in which ZnO and CdO particles are fused into individual nanofibers and assembled into ordered arrays. Optoelectronic and electronic tests revealed that the hybrid NFA behaved as a typical semiconductor while exhibiting improved properties compared to those of the pure ZnO and CdO components. This resulted from the arrangement and the complimentary effects of the components. An array of flexible ZnO-CdO photodetectors with 95% transparency was fabricated on a mica substrate via a one-step process in air. The photodetector revealed a wide spectral range response, high stability, and fast response speed, and in addition, the photodetector performance was not affected even after 200 bending cycles. Taking advantage of the electrospinning process, the composition ratio and the constituents of the nanofiber could be tuned according to various demands. In addition, direction and density of the nanofibers in the array can be well tuned by simply changing the electrospinning setup. Therefore, the final pattern and transparency of the arrays are also adjustable. The advantage of this transfer-free technology is the designed electrospinning method, which simplifies the fabrication process and guarantees a high product quality. The process represents a facile way to fabricate aligned "multicolor" response photodetectors by using predetermined precursors to achieve diverse compositions. We envisage that the reported work paves the way toward efficient photodetector fabrication.

5. Experimental Section

Material Preparation and Characterization: ZnO-CdO nanofiber arrays were fabricated via an improved electrospinning method (SS-2535H, Ucalery). In brief, 1.2 g of polyvinylpyrrolidone (PVP) powder (M_n = 1 300 000) was dissolved in 10 mL of *N*,*N*-dimethylformamide (DMF) solution, then stirred for 10 h at room temperature to obtain a viscogel. Next, 1.0 g of $Zn(CH_3COO)_2{\cdot}2H_2O$ and 1.2 g of $Cd(CH_3COO)_2{\cdot}2H_2O$ (atom ratio of Zn^{2+} and Cd^{2+} is around 1) were added into the PVP/DMF solution to form a uniform liquid as the source. After that, the uniform solution was transferred into a syringe.

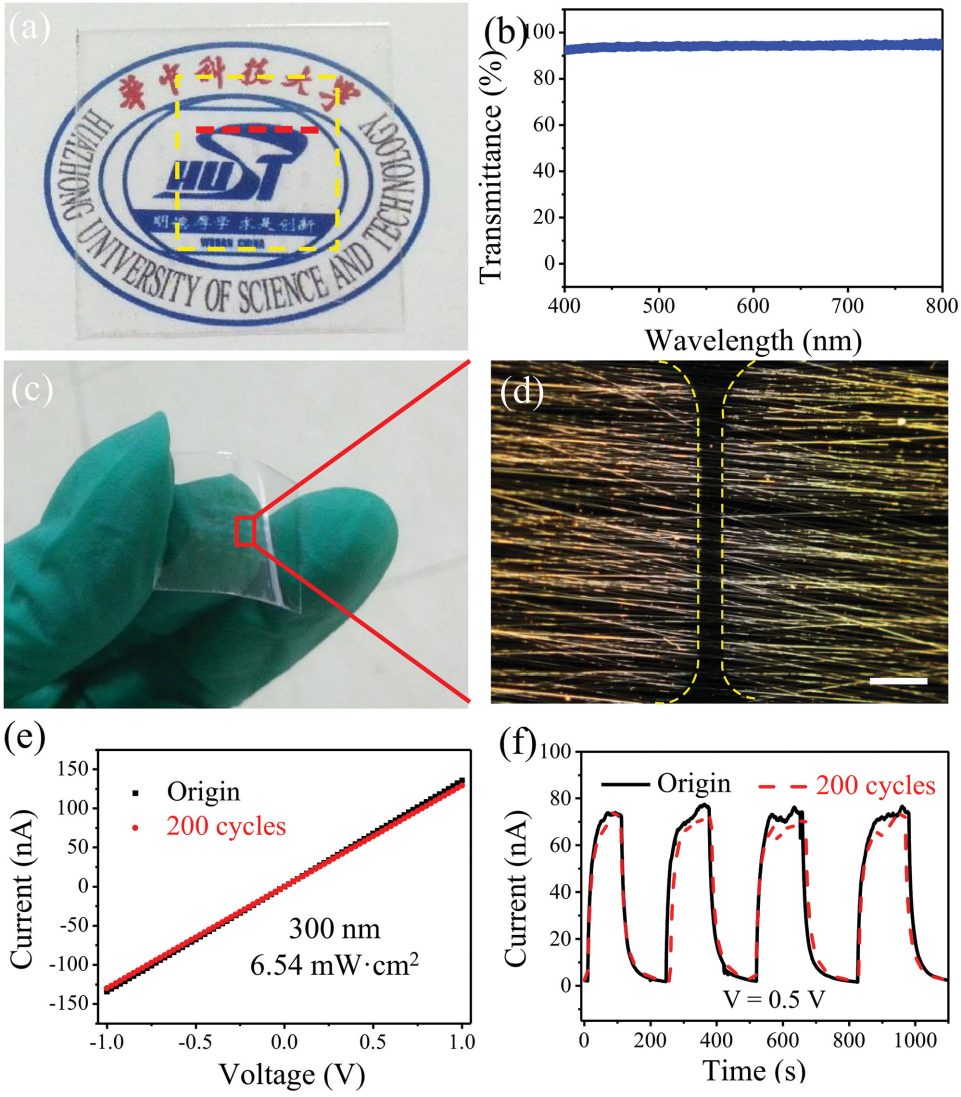

Figure 8. A transparent and flexible photodetector based on the hybrid nanofiber arrays. a) HUST logo covered by the as-fabricated photodetector; the device area is highlighted with a yellow dash rectangle and the rows of the device are highlighted by red rectangles (seven rows in total). b) Optical transmittance of the photodetector. c,d) Bending test of the photodetector made of hybrid arrays. The morphology of the channel is highlighted with yellow dashed lines. The scale bar is 50 μm. e,f) Comparison of current–voltage (*I*–*V*) and current–time (*I*–*t*) curves between the original sample and the sample subjected to 200 bending cycles.

A positive bias from a high-voltage power supply was applied to the needle tip of the syringe, whereas the other terminal was connected to two rectangular aluminum foil contacts that were pasted on a high cure square quartz with a channel width of 10 mm. The distance between the needle tip and the collector was set at 15 cm. The voltages were set to be 8 kV for the positive terminal and 3 kV for the negative terminal. As a result, uniaxially aligned nanofibers of one layer thickness were obtained in the gap. To achieve different array patterns, another pair of aluminum foil contacts could be pasted at different angles, after which the electrospinning process was repeated; as such another layer of uniaxially aligned NFA was stacked on the original layer and formed a hierarchical architecture at different angles. $Zn(CH_3COO)_2$ NFA, $Cd(CH_3COO)_2$ NFA, $Zn(CH_3COO)_2$/PVP and $Cd(CH_3COO)_2$/PVP side-by-side NFA were obtained by electrospinning the Zn ions or Cd ions precursors, respectively. Afterwards, the composite nanofibers were calcined at a rate of 1 °C min^{-1} and kept for 3 h at 500 °C in air. Thus, NFAs made of metal oxides were obtained. The as-prepared oxide nanofiber arrays were characterized by an optical microscope (BX51, OLMPUS), UV-vis spectrometry (U-3900H, Hitachi), X-ray diffraction (XRD, 7000S, Shimadzu), and transmission electron microscopy (TEM, Tecnai G2 F30, FEI and JEM 2100, JEOL) equipped with an X-ray energy dispersive spectrometer (EDS).

Device Fabrication and Characterization: For the nanofiber arrays, the electrodes (Ti/Au (10 nm/100 nm)) were deposited onto the quartz substrate via electron beam (EB) evaporation (Nexdep, Angstrom Engineering) using an Al foil as a shadow mask. The single ZnO-CdO nanofiber device was fabricated by standard photolithography (MDA-400M, Midas), then the Ti/Au (10 nm/100 nm) contacts were deposited over the structure after development. The *I*–*V* characteristics were measured using a low-temperature cryogenic probe station (CRX-6.5K, Lake Shore) and a semiconductor parameter analyzer (4200-SCS, Keithley). A He-Cd laser (IK3301R-G, Kimmon) and a laser-driven white-light source (LDLS, EQ-1500, Energetiq) were used for the measurements of monochromatic 325-nm and wide-range spectral runs between 200 nm and 600 nm, respectively. The light intensity was calibrated using a UV-enhanced Si photodiode.

Supporting Information

Supporting Information is available from the Wiley Online Library or from the author.

Acknowledgements

Z. Zheng and L. Gan contributed equally to this work. This work was supported by the National Nature Science Foundation of China (21322106 and 51472097) and the Ministry of Science and Technology of China (2015CB932600). Y.B. and D.G. are grateful to the International Center for Materials Nanoarchitectonics (MANA) of the NIMS for support. The authors thank the Analytical and Testing Center of Huazhong University of Science and Technology (HUST) for carrying out the XRD, SEM, and HRTEM measurements.

Received: June 19, 2015
Revised: July 24, 2015
Published online: August 27, 2015

[1] T. Zhai, J. Yao, *One-Dimensional Nanostructures: Principles and Applications*, John Wiley & Sons, Hoboken, NJ **2013**.
[2] R. Dong, C. Bi, Q. Dong, F. Guo, Y. Yuan, Y. Fang, Z. Xiao, J. Huang, *Adv. Opt. Mater.* **2014**, *2*, 549.
[3] G. Konstantatos, E. H. Sargent, *Nat. Nanotechnol.* **2010**, *5*, 391.
[4] Y. Xie, M. Gong, T. A. Shartry, J. Lohman, M. C. Hersam, S. Ren, *Adv. Mater.* **2013**, *25*, 3433.
[5] J. Wu, Z. H. Li, D. L. Shao, M. O. Manasreh, V. P. Kunets, Z. M. Wang, G. J. Salamo, B. D. Weaver, *Appl. Phys. Lett.* **2009**, *94*, 102.
[6] L. Li, E. Auer, M. Y. Liao, X. S. Fang, T. Y. Zhai, U. K. Gautam, A. Lugstein, Y. Koide, Y. Bando, D. Golberg, *Nanoscale* **2011**, *3*, 1120.
[7] C. Soci, A. Zhang, B. Xiang, S. A. Dayeh, D. P. R. Aplin, J. Park, X. Y. Bao, Y. H. Lo, D. Wang, *Nano Lett.* **2007**, *7*, 1003.
[8] H. Kind, H. Q. Yan, B. Messer, M. Law, P. D. Yang, *Adv. Mater.* **2002**, *14*, 158.
[9] L. F. Hu, J. Yan, M. Y. Liao, L. M. Wu, X. S. Fang, *Small* **2011**, *7*, 1012.
[10] C. Li, D. H. Zhang, S. Han, X. L. Liu, T. Tang, C. W. Zhou, *Adv. Mater.* **2003**, *15*, 143.
[11] X. S. Fang, L. F. Hu, K. F. Huo, B. Gao, L. J. Zhao, M. Y. Liao, P. K. Chu, Y. Bando, D. Golberg, *Adv. Mater.* **2011**, *21*, 3907.
[12] H. Q. Li, X. Wang, J. Q. Xu, Q. Zhang, Y. Bando, D. Golberg, Y. Ma, T. Y. Zhai, *Adv. Mater.* **2013**, *25*, 3017.
[13] Z. Liu, G. Chen, B. Liang, G. Yu, H. T. Huang, D. Chen, G. Z. Shen, *Opt. Express* **2013**, *21*, 7799.
[14] X. M. Xie, G. Z. Shen, *Nanoscale* **2015**, *7*, 5046.
[15] J. S. Miao, W. D. Hu, N. Guo, Z. Y. Lu, X. M. Zou, L. Liao, S. X. Shi, P. P. Chen, Z. Y. Fan, J. C. Ho, T. X. Li, X. S. Chen, W. Lu, *ACS Nano* **2014**, *8*, 3628.
[16] C. Yang, H. H. Pan, S. Liu, S. Miao, W. H. Zhang, J. S. Jie, X. Xu, *Chem. Commun.* **2015**, *51*, 2593.
[17] L. W. Sang, J. Q. Hu, R. J. Zou, Y. Koide, M. Y. Liao, *Sci. Rep.* **2013**, *3*, 2368.
[18] T. Luo, B. Liang, Z. Liu, X. M. Xie, Z. Lou, G. Z. Shen, *Sci. Bull.* **2015**, *60*, 101.
[19] T. Kuykendall, P. Ulrich, S. Aloni, P. D. Yang, *Nat. Mater.* **2007**, *6*, 951.
[20] G. Ariyawansa, M. B. M. Rinzan, M. Alevli, M. Strassburg, N. Dietz, A. G. U. Perera, S. G. Matsik, A. Asghar, I. T. Ferguson, H. Luo, A. Bezinger, H. C. Liu, *Appl. Phys. Lett.* **2006**, *89*, 091113.
[21] S. C. Rai, K. Wang, J. J. Chen, J. K. Marmon, M. Bhatt, S. Wozny, Y. Zhang, W. L. Zhou, *Adv. Electron. Mater.* **2015**, *1*, 1400050.
[22] L. F. Hu, J. Yan, M. Y. Liao, H. J. Xiang, X. G. Gong, L. D. Zhang, X. S. Fang, *Adv. Mater.* **2012**, *24*, 2305.
[23] J. Yoo, S. Jeong, S. Kim, J. H. Je, *Adv. Mater.* **2015**, *27*, 1712.
[24] X. Gong, M. Tong, Y. Xia, W. Cai, J. S. Moon, Y. Cao, G. Yu, C.-L. Shieh, B. Nilsson, A. J. Heeger, *Science* **2009**, *325*, 1665.
[25] M. S. Arnold, J. D. Zimmerman, C. K. Renshaw, X. Xu, R. R. Lunt, C. M. Austin, S. R. Forrest, *Nano Lett.* **2009**, *9*, 3354.
[26] T. Y. Zhai, L. Li, Y. Ma, M. Y. Liao, X. Wang, X. S. Fang, J. N. Yao, Y. Bando, D. Golberg, *Chem. Soc. Rev.* **2011**, *40*, 2986.
[27] C. L. Zhang, S. H. Yu, *Chem. Soc. Rev.* **2014**, *43*, 4423.
[28] D. Li, Y. N. Xia, *Adv. Mater.* **2004**, *16*, 1151.
[29] Y. Z. Long, M. Yu, B. Sun, C. Z. Gu, Z. Y. Fan, *Chem. Soc. Rev.* **2012**, *41*, 4560.
[30] S. H. Choi, G. Ankonina, D. Y. Youn, S. G. Oh, J. M. Hong, A. Rothschild, II- D. Kim, *ACS Nano* **2009**, *3*, 2623.
[31] Y. Q. Liu, X. P. Zhang, Y. N. Xia, H. Yang, *Adv. Mater.* **2010**, *22*, 2454.
[32] J. W. Xie, W. Y. Liu, M. R. MacEwan, P. C. Bridgman, Y. N. Xia, *ACS Nano* **2014**, *8*, 1878.
[33] T. Y. Zhai, L. Li, X. Wang, X. S. Fang, Y. Bando, D. Golberg, *Adv. Funct. Mater.* **2010**, *20*, 4233.
[34] Z. Liu, J. Xu, D. Chen, G. Z. Shen, *Chem. Soc. Rev.* **2015**, *44*, 161.
[35] S. Y. Min, T. S. Kim, B. J. Kim, H. Cho, Y. Y. Noh, H. Yang, J. H. Cho, T. W. Lee, *Nat. Commun.* **2013**, *4*, 1773.
[36] X. Liu, L. L. Gu, Q. P. Zhang, J. Y. Wu, Y. Z. Long, Z. Y. Fan, *Nat. Commun.* **2014**, *5*, 4007.
[37] a) D. Li, Y. L. Wang, Y. N. Xia, *Nano Lett.* **2003**, *3*, 1167; b) D. Li, Y. L. Wang, Y. N. Xia, *Adv. Mater.* **2014**, *16*, 361.
[38] L. Li, P. S. Lee, C. Y. Yan, T. Y. Zhai, X. S. Fang, M. Y. Liao, Y. Bando, D. Golberg, *Adv. Mater.* **2010**, *22*, 5145.
[39] W. Tian, C. Zhang, T. Y. Zhai, S. L. Li, X. Wang, J. W. Liu, X. Jie, D. Q. Liu, M. Y. Liao, Y. Koide, D. Golberg, Y. Bando, *Adv. Mater.* **2014**, *26*, 3088.
[40] W. Tian, T. Y. Zhai, C. Zhang, S.-L. Li, X. Wang, F. Liu, D. Q. Liu, X. K. Cai, K. Tsukagoshi, D. Golberg, Y. Bando, *Adv. Mater.* **2013**, *25*, 4625.
[41] B. Sun, Y. Z. Long, S. L. Liu, Y. Y. Huang, J. Ma, H. D. Zhang, G. Z. Shen, S. Xu, *Nanoscale* **2013**, *5*, 7041.
[42] H. Kind, H. Q. Yan, B. Messer, M. Law, P. D. Yang, *Adv. Mater.* **2002**, *14*, 158.
[43] C. L. Lai, X. X. Wang, Y. Zhao, H. Fong, Z. T. Zhu, *RSC Adv.* **2013**, *3*, 6640.
[44] Y. B. Li, F. D. Valle, M. Simonnet, I. Yamada, J.-J. Delaunay, *Appl. Phys. Lett.* **2009**, *94*, 023110.
[45] G. Y. Chai, L. Chow, O. Lupan, E. Rusu, G. I. Stratan, H. Heinrich, V. V. Ursaki, I. M. Tiginyanu, *Solid State Sci.* **2011**, *13*, 1205.
[46] J. Q. Xu, Y. Y. Chang, L. Gan, Y. Ma, T. Y. Zhai, *Adv. Sci.* **2015**, *2*, 1500023.
[47] C. C. Lien, C. Y. Wu, Z. Q. Li, J. J. Lin, *J. Appl. Phys.* **2011**, *110*, 063706.
[48] W. E. Mahmoud, A. A. Al-Ghamdi, F. El-Tantawy, S. Al-Heniti, W. E. Mahmoud, *J. Alloys Compd.* **2009**, *485*, 59.
[49] H. Wu, D. S. Kong, Z. C. Ruan, P.-C. Hsu, S. Wang, Z. F. Yu, T. J. Carney, L. B. Hu, S. H. Fan, Y. Cui, *Nat. Nanotechnol.* **2013**, *8*, 421.
[50] A. Facchetti, T. J. Marks, *Transparent Electronics from Synthesis to Applications*, Wiley, Chichester, West Sussex, UK **2010**.
[51] G. Chen, B. Liang, X. Liu, Z. Liu, G. Yu, X. Xie, T. Luo, D. Chen, M. Q. Zhu, G. Z. Shen, Z. Y. Fan, *ACS Nano* **2014**, *8*, 787.
[52] Q. S. Wang, K. Xu, Z. X. Wang, F. Wang, Y. Huang, M. Safdar, X. Y. Zhan, F. M. Wang, Z. Z. Cheng, J. He, *Nano Lett.* **2015**, *15*, 1183.